scientific reports

Check for updates

OPEN

Spectrometer-free time-division multiplexed NIR time-of-flight vision system for visually similar material recognition

Tae-In Jeong[1,4], Jae-Young Kim[1,4], Eunji Choi[1,4], San Kim[1], Sehyeon Kim[1], Munki Song[1], Junho Lee[2], Alexander Gliserin[1,2], Robert A. Taylor[3] & Seungchul Kim[1,2]✉

Conventional machine vision systems based on RGB cameras struggle to distinguish materials that appear visually identical, such as plastics of the same color and shape. To address this limitation, we present a spectrometer-free time-division multiplexed (TDM) near-infrared (NIR) time-of-flight (ToF) vision system that enables simultaneous acquisition of spectral and geometric information using dual-detector architecture composed of an avalanche photodiode (APD) for multispectral reflectance detection and a single-photon avalanche diode (SPAD) for ToF ranging. By extending TDM to multispectral NIR imaging, the proposed system temporally separates nanosecond laser pulses at 980 nm, 1450 nm, and 1650 nm for material discrimination, while an additional 905 nm channel provides high-precision ToF depth mapping. This architecture eliminates bulky spectrometers and dispersive optics, minimizing optical loss while maintaining compactness and scalability. The system successfully recognizes 12 visually similar materials, including six white plastics, three green rubbers, and three silver metals, based on their unique NIR reflectance fingerprints encoded into false-color RGB images. A convolutional neural network (CNN) trained on these images achieves near-perfect classification accuracy. Furthermore, a dual-domain experiment with a mannequin and a human subject demonstrates simultaneous reconstruction of surface geometry and material differentiation under realistic conditions. This spectrometer-free multispectral ToF vision approach establishes a compact and efficient sensing platform for high-precision robotic perception, intelligent manufacturing, and physical artificial intelligence systems requiring both spectral and spatial awareness.

Keywords Machine vision, Multispectral vision system, Time division multiplexing, Time of flight

Machine vision systems have rapidly advanced across diverse fields, including automated manufacturing, robotics, and intelligent inspection. These developments have been largely driven by vision-based measurement (VBM) techniques, which integrate vision sensors, electronics, and computational algorithms[1]. The rise of artificial intelligence (AI), particularly machine learning (ML)-based classification and recognition methods, has significantly enhanced image analysis capabilities, improving the accuracy, reliability, and speed of measurement systems[2–7]. Consequently, VBM has evolved from a simple image-processing approach into an essential tool for modern instrumentation and automation.

Despite these advances, most existing vision systems still rely on RGB cameras, which provide only color and geometric information. This limits their ability to capture intrinsic material characteristics and fine surface geometry[8–11]. RGB-D sensors partially alleviate this limitation by integrating active depth sensing, yet the mismatch between RGB and depth-map resolutions, along with insufficient spectral information, hinders their effectiveness in distinguishing visually similar materials[12]. Polarization-sensitive imaging has also been investigated as a useful modality for distinguishing visually similar materials by providing additional contrast

[1]Department of Cogno-Mechatronics Engineering, College of Nanoscience and Nanotechnology, Pusan National University, Busan 46241, Republic of Korea. [2]Department of Optics and Mechatronics Engineering, College of Nanoscience and Nanotechnology, Pusan National University, Busan 46241, Republic of Korea. [3]Department of Physics, University of Oxford, Oxford, UK. [4]Tae-In Jeong, Jae-Young Kim and Eunji Choi contributed equally to this work. ✉email: s.kim@pusan.ac.kr

related to scattering and surface optical properties[13,14]. Accurate and reliable acquisition of both material and geometric information remains a critical requirement for high-precision object recognition in production lines, recycling systems, and humanoid robotics[15–18].

The use of NIR lights (900–2500 nm) has emerged as a promising technique due to its rich material-dependent reflection and absorption features, which are more sensitive to molecular composition[19–23]. Multispectral and hyperspectral imaging in the NIR range has demonstrated high effectiveness in identifying material characteristics, enabling more precise discrimination than visible-light imaging[20,24–27]. However, these techniques typically rely on incoherent light sources, leading to low measurement efficiency and the inability to simultaneously capture depth information[28–31]. NIR multispectral LiDAR systems have recently been developed to overcome these limitations by employing coherent pulsed laser sources that provide high signal-to-noise ratios (SNRs) and enable simultaneous spectral and distance measurements[32–35]. Nevertheless, conventional architectures depend on complex dispersive optics including diffraction gratings and multiple detectors[36–38] that introduce optical loss and alignment issues, thereby reducing measurable range and overall system performance[39,40].

In this study, we propose a spectrometer-free TDM based ToF vision system that enables simultaneous acquisition of spectral and depth information through two physically separated detection paths, consisting of an avalanche photodiode (APD) for multispectral signal acquisition and a single-photon avalanche diode (SPAD) for ToF ranging. Building upon our previous work[41], which introduced simultaneous acquiring both distance and material information using a TDM based approach without complex spectroscopic configurations, we developed an advanced system and exploited this technique to recognize visually similar 12 materials (Polypropylene, Acrylonitrile Butadiene Styrene, Polystyrene, Polyoxymethylene, Polytetrafluoroethylene, Polyethylene, Ethylene Propylene Diene Monomer, Polyvinyl Chloride, Silicon, Iron, Magnesium, Stainless Steel) that shares the same geometry and color. These materials were grouped into three visually similar categories: six white plastics, three green rubbers, and three silver metals. The collected multispectral NIR data are converted into false-color RGB images based on a wavelength-to-color mapping scheme, enabling intuitive visualization of material-dependent spectral features. A convolutional neural network (CNN) model trained on these false-color RGB images containing the spectral fingerprints of 12 different materials not only successfully classified the materials but also demonstrated generalization capability by accurately identifying objects with different shapes composed of the same material. The classification process was validated through uncertainty analysis in accordance with the guide to the expression of uncertainty in measurement (GUM)[42]. A dual-domain experiment involving a mannequin and a human subject further validates the system's ability to reconstruct 3D geometry while distinguishing material types under realistic conditions. Statistical analysis of repeated depth measurements confirms the high ranging precision and stability of the proposed method. Overall, the presented TDM-based NIR ToF vision system establishes a compact, high-speed, and high-precision dual-domain sensing platform capable of spectrometer-free material and geometry recognition. This approach holds promise for advanced applications in robotic vision, smart manufacturing, and physical AI frameworks, where integrated spectral and spatial awareness can significantly enhance the intelligence and adaptability of autonomous systems.

Results and discussion

Principle of the time division multiplexing (TDM) based real-time multispectral vision system

TDM is a technique in data communication that enables multiple data streams to share a single transmission channel[43]. TDM enables accurate and efficient sequential transmission of signals, by assigning predefined time slots to each stream under a common data clock and maintaining precise synchronization between transmitter and receiver[44,45]. By extending the concept of TDM to spectroscopy, spectral components can be temporally separated using synchronized trigger signals driven by a system clock. This enables the multispectral NIR reflectance signals to be acquired through a single broadband APD in the spectroscopic detection path. Compared to conventional spectroscopic imaging techniques that rely on complex spectrally resolved detector arrays, this approach provides a significantly more compact and hardware efficient alternative. Furthermore, by incorporating ToF measurements within the synchronization framework, TDM-based multispectral imaging systems can simultaneously acquire both spectral and distance information, enabling integrated analysis of material composition and structural geometry. The operating principle of the proposed TDM-based multispectral vision system is schematically illustrated in Fig. 1. The system employs two physically separated receiving paths, consisting of an InGaAs APD for multispectral reflectance detection and a Si-based SPAD for ToF acquisition. For precise distance imaging, a 905 nm ToF laser with a pulse width of a few nanoseconds was employed, while spectroscopic imaging was performed using three lasers at 980 nm, 1450 nm, and 1650 nm, each with a pulse width of 100 ns. The 905 nm wavelength was selected for the ToF channel because it can be efficiently detected with a Si-based SPAD, enabling high sensitivity and excellent time resolution for precise distance acquisition. In contrast, the 980, 1450, and 1650 nm wavelengths were selected as a minimal set for spectral analysis to capture material-dependent reflectance differences in the NIR region while limiting the number of combined beams and the associated optical loss in the beam combining process. The four laser channels were precisely synchronized by a 500 kHz clock signal and sequentially triggered with 200 ns intervals to prevent temporal overlap between wavelengths. Dichroic long pass filters were utilized to combine the four nanosecond pulse lasers, minimizing the use of beam splitters in order to reduce optical loss. The combined four nanosecond laser pulse trains were directed onto a galvano mirror, and scanning was performed over a field of view of approximately 60° in the horizontal direction and 10° in the vertical direction, with 16,000 pixels per frame (configured as a 40 × 400 array) at a galvano scanning rate of 10 Hz. Since one scanning cycle was used for system initialization, the effective image acquisition rate was 9 Hz, while the single-frame acquisition time for a 40 × 400 image was 100 ms. Given that the TDM-based architecture necessitates nanosecond-scale time-domain processing, full-frame acquisition generates a substantial volume of time-resolved data. To ensure

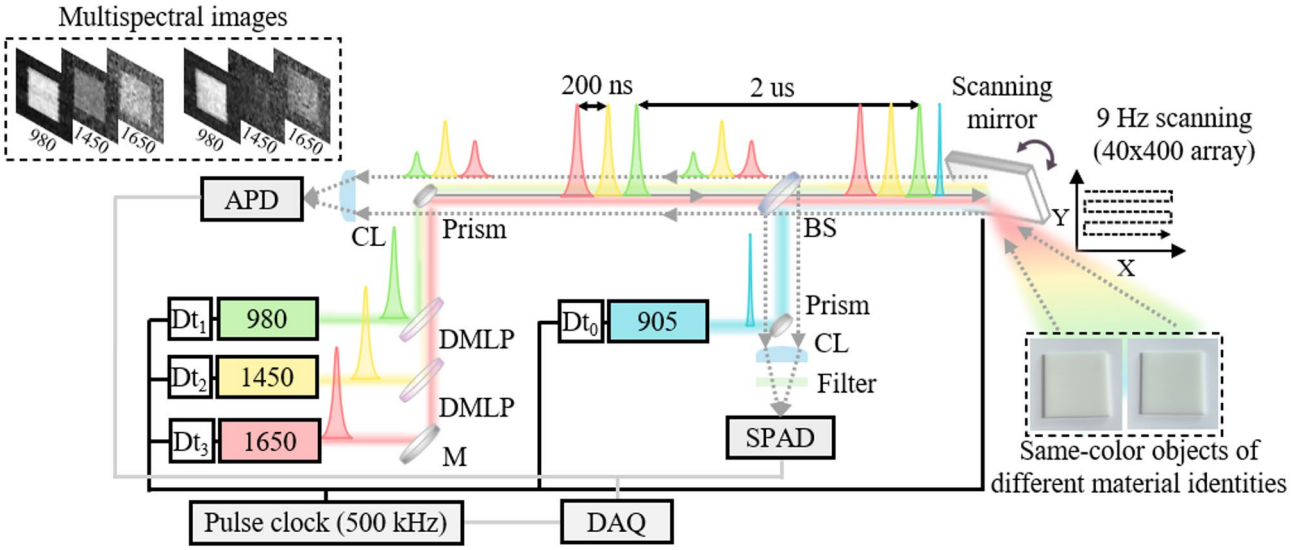

Fig. 1. Principle of the TDM based real-time multispectral imaging system for object material classification based on NIR spectral fingerprinting. Three difference wavelength (980 nm, 1450 nm, and 1650 nm) of nanosecond(ns) pulse laser utilized for material classification and one wavelength (905 nm) utilized for ToF calculation. APD: Avalanche photodiode; SPAD: Single-photon Avalanche diode; DAQ: Data acquisition; DMLP: Dichroic mirror long pass; CL: Collection lens; BS: Beam splitter; M: Mirror.

stable real-time operation, we implemented a time-gated acquisition scheme synchronized with the ToF trigger, allowing the intensity of each wavelength to be extracted from its designated temporal window. Under these conditions, the current spatial resolution was optimized as a practical trade-off to maintain robust real-time multispectral imaging. Each wavelength of the reflected pulses was acquired sequentially with a synchronized emission and scanning system. This configuration enables the acquisition of spatially identical spot information, unlike conventional RGB-D sensors, which suffer from viewpoint discrepancy limitations. To enable effective material discrimination, the amplitude ratios of reflected pulses at different wavelengths are used as distinctive spectral fingerprints, which requires the accurate and stable acquisition of high SNR reflectance spectra. A dual-domain measurement architecture was implemented to enable both accurate ranging and reliable spectral acquisition. In addition, to minimize optical losses and improve light collection efficiency, a prism matched to the size of the collimated beam was used instead of a beam splitter. In this system, the reflected pulses train is focused on an InGaAs APD for spectroscopic analysis, while a portion of the signal is simultaneously directed to a silicon-based SPAD for ToF signal measurement. A 905 nm bandpass filter was placed in front of the SPAD to selectively detect the ToF signal, enabling precise distance measurement.

False-color RGB encoding data process of multispectral image

To validate the material recognition performance of the TDM-based multispectral vision system, square plates samples with dimensions of 10 cm × 10 cm, prepared from 12 different materials, including plastics, rubber, and metals, were selected as target samples. The surface appearance and average RGB values of each sample were analyzed (Fig. 2a). Although the samples differ in material composition, they exhibit highly similar visible colors and closely matched RGB values in the visible spectrum. This highlights the limitations of conventional RGB imaging in material classification and emphasizes the need for spectral information beyond the visible range. The reflection spectra of 12 different target samples were measured in NIR range. For precise reflection spectrum measurement and analysis, the measured spectrum was calibrated using a wavelength-dependent scaling factor defined as the ratio between the reference spectrum of the tungsten-halogen lamp (HL-2000, Ocean Optics) and the spectrum measured by NIR spectrometer (Flame-NIR, Ocean Optics), $S(\lambda) = I_{\mathrm{ref}}(\lambda)/I_{\mathrm{meas}}(\lambda)$. The calibrated spectrum was then obtained as $I_{\mathrm{cal}}(\lambda) = I_{\mathrm{sample,\,meas}}(\lambda) \times S(\lambda)$, and the corresponding scaling factors are presented in Fig. S1. The calibrated reflection spectrum exhibited clearly distinguishable differences among the materials, showing that the three wavelengths used in the TDM-based multispectral vision system (980 nm, 1450 nm and 1650 nm) effectively capture material-specific reflectance fingerprints (Fig. 2b). The grayscale intensity maps acquired through the TDM-based multispectral vision system inherently contain material specific spectroscopic fingerprints. To enable intuitive visualization of these spectral fingerprints, RGB-color encoding was applied to the grayscale intensity maps of three selected wavelengths, with the measured NIR reflectance intensities at 980, 1450, and 1650 nm assigned to the R, G, and B channels, respectively (Fig. 3a). In this paper, the a false-color RGB image refers to an image reconstructed from multispectral NIR reflectance data, distinguishing them from conventional visible-light RGB images. Because the false-color RGB image is reconstructed by combining the intensity maps of three selected NIR wavelength channels, local fluctuations in each channel can appear as high-frequency color variations in the final image. Accordingly, the mosaic-like appearance observed in the false-color image arises from the RGB encoding process of the multispectral intensity

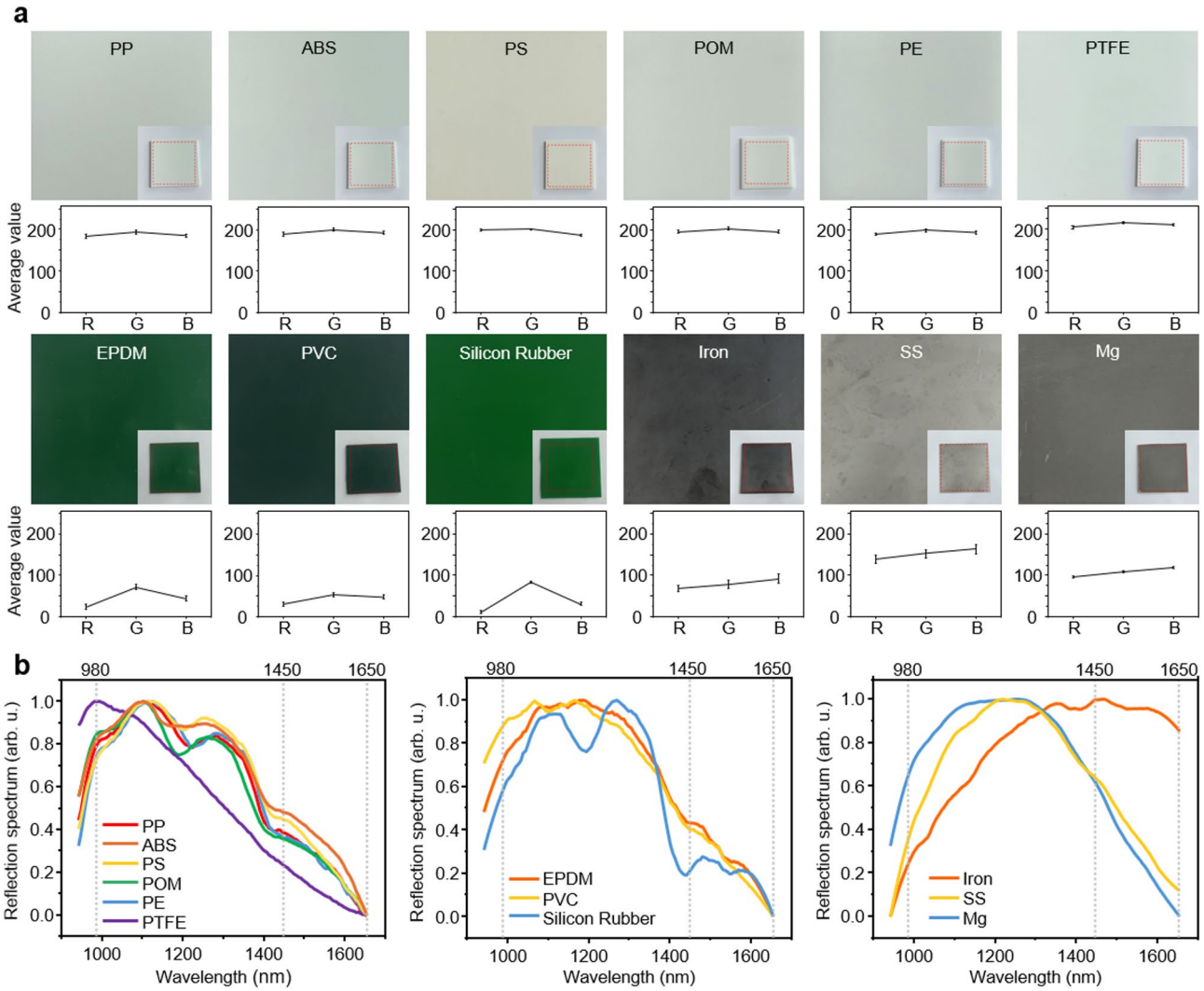

Fig. 2. (**a**) Surface images and average RGB values (R: red, G: green, B: blue). (**b**) corresponding NIR reflection spectra of 12 target materials, categorized by color: six white-colored polymers (PP, ABS, PS, POM, PE, PTFE), three green-colored materials (EPDM, PVC, Silicon Rubber), and three silver-colored metals (Iron, SS, Mg). PP: Polypropylene; ABS: Acrylonitrile Butadiene Styrene; PS: Polystyrene; POM: Polyoxymethylene; PE: Polyethylene; PTFE: Polytetrafluoroethylene; EPDM: Ethylene Propylene Diene Monomer; PVC: Polyvinyl Chloride; SS: Stainless Steel; Mg: Magnesium.

maps, while the material-dependent spectral fingerprints remain preserved for discrimination. The resulting false-color RGB image facilitates effective material discrimination, not only through human visual perception but also through machine learning based classification algorithms. For precise false-color RGB encoding, wavelength-specific calibration factors were determined using an NIR reference board (EDI CORPORATION) with a reference reflectance spectrum measured by a calibrated spectrophotometer (LAMBDA 950, PerkinElmer), as shown in Fig. 3b. The reference board was then imaged using the TDM-based multispectral vision system, and the average grayscale intensity within the region of interest (ROI) was extracted at each wavelength (Fig. 3c). By comparing the measured ROI intensity with the corresponding reference reflectance, a wavelength-dependent response value was obtained for each channel. These response values were then normalized relative to one another to compensate for channel-to-channel response differences among the selected wavelengths. The resulting scaling factors were applied during the false-color RGB encoding process to correct wavelength-dependent discrepancies arising from variations in laser output power and detector sensitivity. The false-color RGB images were generated for 12 different target materials, and the resulting color variations among the materials reflect their distinct spectral fingerprints (Fig. 3d). These color differences, though subtle in the visible domain, enable reliable discrimination of materials even when the material appears similar in shape and color. Additionally, four samples with identical materials and geometry but differing in visible color were prepared to demonstrate that the system captures material characteristics independently of color variations in the visible spectrum (Fig. S2a). The resulting false-color RGB images showed consistent spectral patterns across all samples,

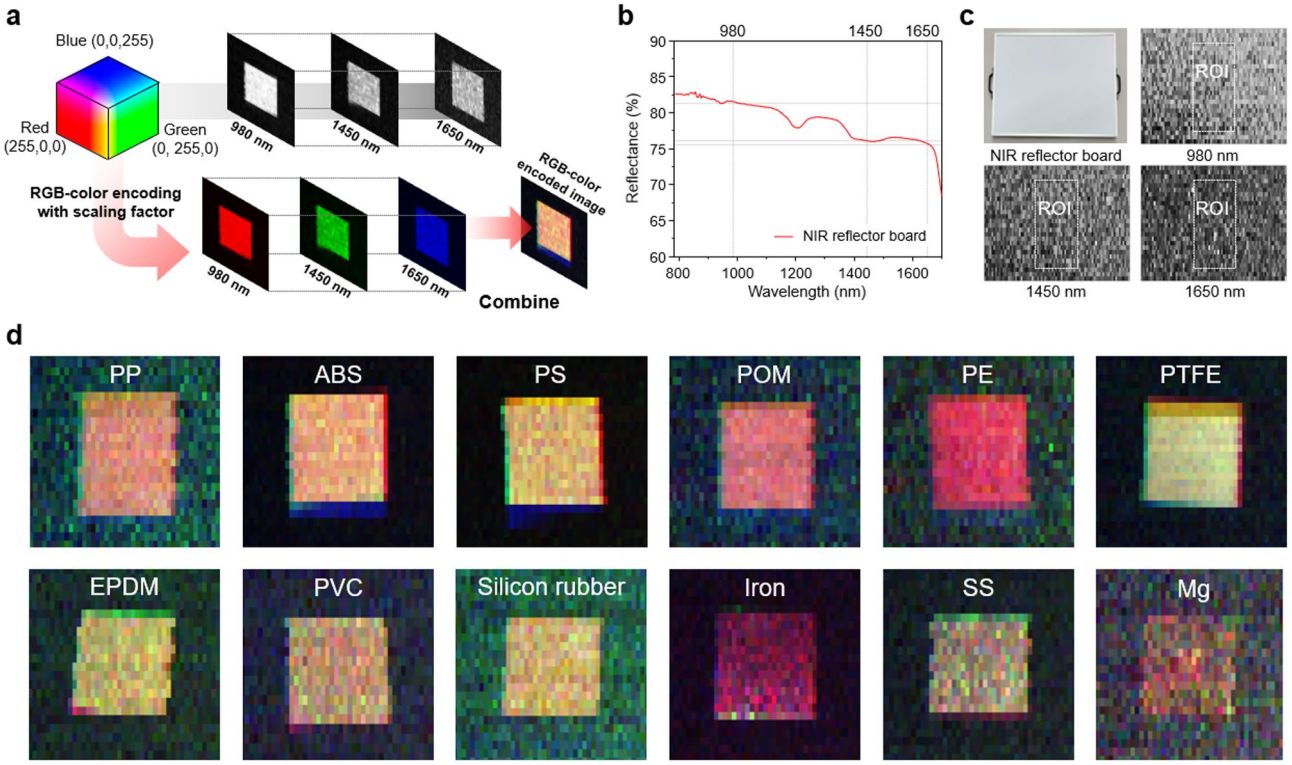

Fig. 3. False-color RGB visualization of multispectral NIR data for various materials. (**a**) Principle of false-color multispectral image processing, in which the measured NIR reflectance intensities at 980, 1450, and 1650 nm are assigned to the R, G, and B channels, respectively. (**b**) Reflectance spectrum of NIR reflection board for spectral calibration of TDM-based multispectral vision system. (**c**) NIR reflection board and measured results via TDM-based multispectral vision system for spectral calibration of imaging system. (**d**) False-color RGB images of 12 different materials at a distance of 2.5 m, generated from the multispectral NIR reflectance maps.

confirming that the proposed TDM-based multispectral vision system is robust to changes in visible color while remaining highly sensitive to intrinsic material properties (Fig. S2b).

Multispectral material species classification using a CNN model

CNN has demonstrated outstanding performance in image classification, object detection, and semantic segmentation, owing to its ability to extract hierarchical spatial features using shared convolutional kernels[46,47]. The 12 target materials are visually similar in the visible spectrum as white, green, and silver objects but exhibit distinct spectral fingerprints in the NIR range. These spectral characteristics are effectively captured using a TDM approach and are intuitively embedded in false-color RGB images, enabling accurate classification through a CNN model. In this study, the CNN primarily learns wavelength-dependent relative response patterns represented in the false-color multispectral images, rather than relying on fine spatial texture. Therefore, even under limited spatial resolution, material classification remains feasible as long as the material-dependent spectral contrast among the three NIR channels is preserved. To ensure that the training data reflect a broader range of realistic measurement conditions, each material was measured under multiple orientations and positions relative to the optical axis. The CNN architecture was trained on a dataset comprising 12,000 false-color RGB image generated from multispectral NIR reflectance maps representing 12 distinct materials. The dataset was divided into training (80%), validation (10%), and test (10%) subsets using stratified random sampling to preserve the class distribution across all material categories, thereby ensuring robust generalization and preventing overfitting through adequate validation. Prior to training, all RGB images were resized to 512 × 512 pixels and normalized by rescaling the pixel values to the range of 0 to 1. The CNN model consisted of three convolutional layers with 64, 32, and 32 filters, respectively, each using a 3 × 3 kernel with a ReLU activation function, followed by a 2 × 2 max-pooling layer. After flattening, a fully connected layer with 256 units and ReLU activation was applied, followed by a dropout layer with a rate of 0.3 to prevent overfitting. The final dense layer consisted of 12 units with a softmax activation function for material classification (Fig. 4a). The network was trained using the Adam optimizer with a learning rate of 0.0001, a batch size of 32, and categorical cross-entropy loss. The training time of the CNN model was accelerated by utilizing parallel computation with NVIDIA CUDA on an NVIDIA GeForce RTX 3050 graphics processing unit (GPU). Training the entire model takes approximately 1.5 hours, while classifying new data requires only 0.2 second per sample in the trained model, ensuring sufficient efficiency for real-time applications. The loss and accuracy curves represent the learning process of the CNN,

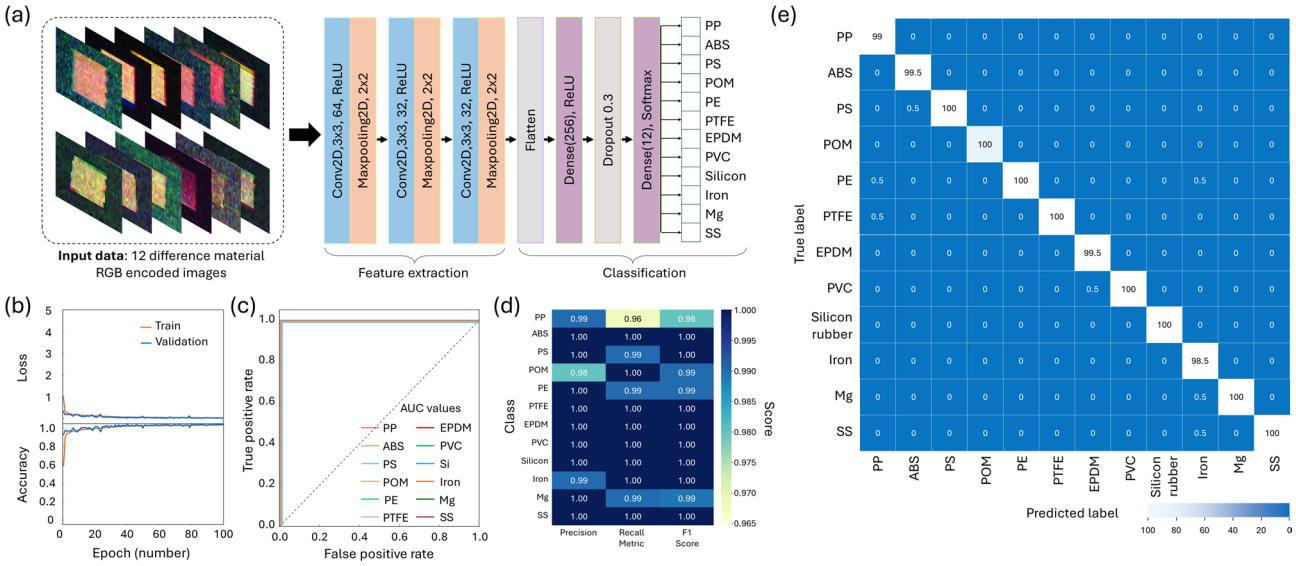

Fig. 4. Material classification of multispectral images via the CNN platform. (**a**) Schematic of the CNN model training process with multispectral images. (**b**) Loss and accuracy values for each epoch for the training (orange lines) and validation (blue lines) data. (**c**) ROC curves and their AUC values. (**d**) Precision, Recall metric, and F1 score of trained model. (**e**) Confusion matrix values of the labeled and predicted material species.

including the training and the validation part (Fig. 4b). As training progresses, loss and accuracy curve converge steadily toward 0 and 1, respectively, with no into training and validation sets. The classifier performance was evaluated using the receiver operating characteristic (ROC) curve, which compares the true positive rate against the false positive rate (Fig. 4c). Our optimized CNN model achieved a perfect area under the curve (AUC) of 1, indicating that the model reliably classified all 12 different materials without error. The trained model exhibited outstanding classification performance across all evaluation metrics, including precision, recall, and F1 score (Fig. 4d). A confusion matrix represents the distribution of the model's predictions across true labels, with each cell indicating the percentage of samples classified into a particular category (Fig. 4e). The principal diagonal values represent the percentage of correctly classified samples for each class. The accuracy was calculated as the ratio of correctly predicted samples to the total number of validation samples. The results demonstrate the model's capability to accurately classify material species. Furthermore, to evaluate the model's robustness and its ability to generalize well across different datasets, k-fold cross-validation was performed. The results showed consistently outstanding performance across the different data partitions (Fig. S3). To evaluate the uncertainty of the CNN model, we implemented the Monte Carlo Dropout method in accordance with the GUM, which applies dropout not only during training but also at run time, introducing randomness into the prediction process. Consequently, the network produces different outputs for the same input depending on the nodes that are randomly dropped out[42]. By applying the model's existing dropout layer (rate = 0.3) at run-time and performing T = 50 forward passes over the entire test set, we obtained a predictive distribution for each classification. The mean of these distributions was used as the final prediction, achieving a robust test accuracy of 98.95% with standard deviation 0.0229. This very low standard deviation provides model's low uncertainty and statistically reinforces its reliability for material recognition. These various evaluation results of the CNN model demonstrate that our TDM-based multispectral vision system and data processing method enable highly accurate and reliable material recognition. These results further suggest that the CNN primarily learns material-dependent relative response patterns represented in the false-color multispectral images, rather than relying solely on fine spatial texture or image-specific statistical fluctuations. In particular, the consistently strong performance observed in k-fold validation and Monte Carlo dropout analysis supports the robustness of the learned multispectral features under the present imaging condition.

To evaluate the generalization performance of the model, additional POM and PE samples were prepared in rod geometries distinct from those used during training, with a diameter of 1 cm and a length of 30 cm (Fig. 5a). These samples were measured under the same experimental condition to ensure consistency, and their false-color RGB image were obtained respectively (Fig. 5b). As shown in the confusion matrix, the pretrained CNN model correctly classified all the rod geometries POM and PE samples (Fig. 5c). This result demonstrates that the proposed system maintains high classification accuracy for previously unseen samples with variations in geometry and fabrication conditions, indicating that the network learns material-dependent multispectral characteristics rather than being limited to the specific sample geometry or image pattern present in the training set.

Additionally, baseline comparisons using support vector machine (SVM) and random forest were performed on the same RGB-encoded multispectral dataset, and the classifier performance was evaluated using confusion matrices, as shown in Fig. S4. Both baseline classifiers exhibited strong classification performance with confusion

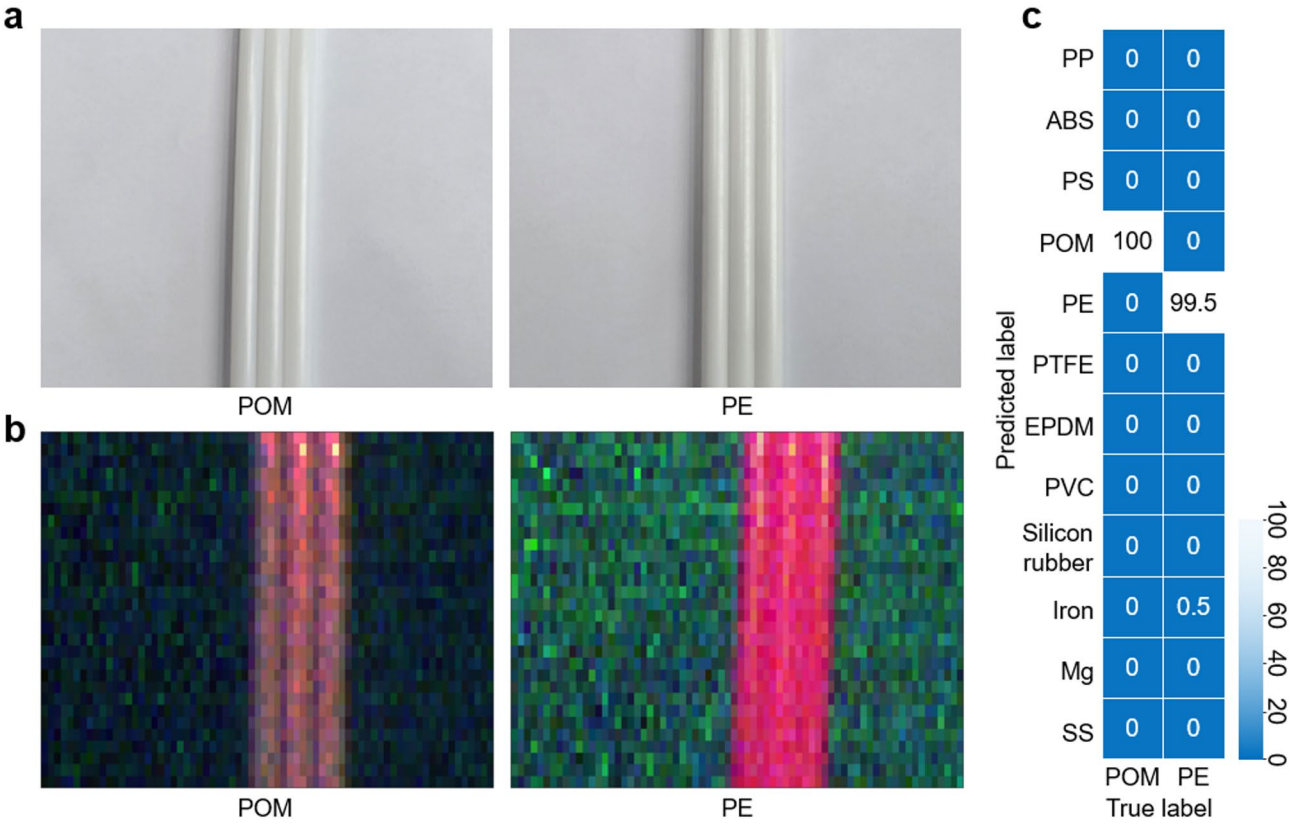

Fig. 5. Material classification of multispectral images via the pretrained CNN model. (**a**) The image of 2 different materials of white color plastic (POM, PE). (**b**) Corresponding multispectral false-color RGB images. (**c**) Confusion matrix value of true and predicted material species.

patterns comparable to those of the CNN. These results indicate that the proposed false-color RGB-encoded multispectral image representation effectively captures material-dependent spectral response characteristics. In other words, the strong classification performance is not solely dependent on a specific CNN architecture, but is also supported by the discriminative information preserved through the proposed TDM-based multispectral sensing and RGB encoding process.

Demonstration of dual domain detection in material characteristic and range

The TDM-based multispectral vision system is designed not only for multispectral imaging but also for simultaneous acquisition of distance information through ToF measurements. This is achieved by calculating the ToF between the transmitted trigger pulse used to laser emission and the corresponding reflected pulse received from the object. To demonstrate the dual-domain sensing capability of the proposed system, encompassing both spectroscopic material characterization and distance measurement, experiment was conducted at a distance of 5 m using a mannequin and a human subject. In order to evaluate the system under a real-world scenario where visual distinction is challenging, two different targets of the human subject and the mannequin were placed in identical poses and dressed in clothing made of the same material (Fig. 6a). For clearer comparison, only the ROI corresponding to the targets were extracted and visualized from the full measurement field. The ToF based distance map not only visualizes the distance difference between the mannequin and the background wall, but also accurately captures the detailed 3D shape and surface curvature of key body parts such as the torso, arms, and neck. This result demonstrates that the proposed system is capable of high-resolution reconstruction of fine geometric features, extending beyond simple range measurement (Fig. 6b). To evaluate the repeatability of the distance measurement, experiments were conducted on several ROIs with 130 repeated measurements. The measurement repeatability, quantified as the standard deviation, was as low as 7.359 mm, 9.782 mm, and 12.19 mm for the respective ROIs on the target surfaces, with average distances of 4.667 m, 4.677 m, and 5.204 m, respectively (Table S1). This low standard deviation demonstrates the high precision and stability of the proposed system. The false-color RGB image clearly visualizes the surface material difference between human skin and the mannequin based on their distinct spectral reflectance characteristics in the NIR region. Even under conditions of identical visible appearance, the inherent spectral differences between the materials are captured and reflected in the encoded color output, enabling intuitive distinction. This result demonstrates that the proposed system effectively identifies material characteristics that are indistinguishable with conventional RGB cameras (Fig. 6c). A dual domain combined output was additionally generated by integrating the ToF based distance map with the false-color RGB image, thereby embedding both geometric and material characteristics within a single data

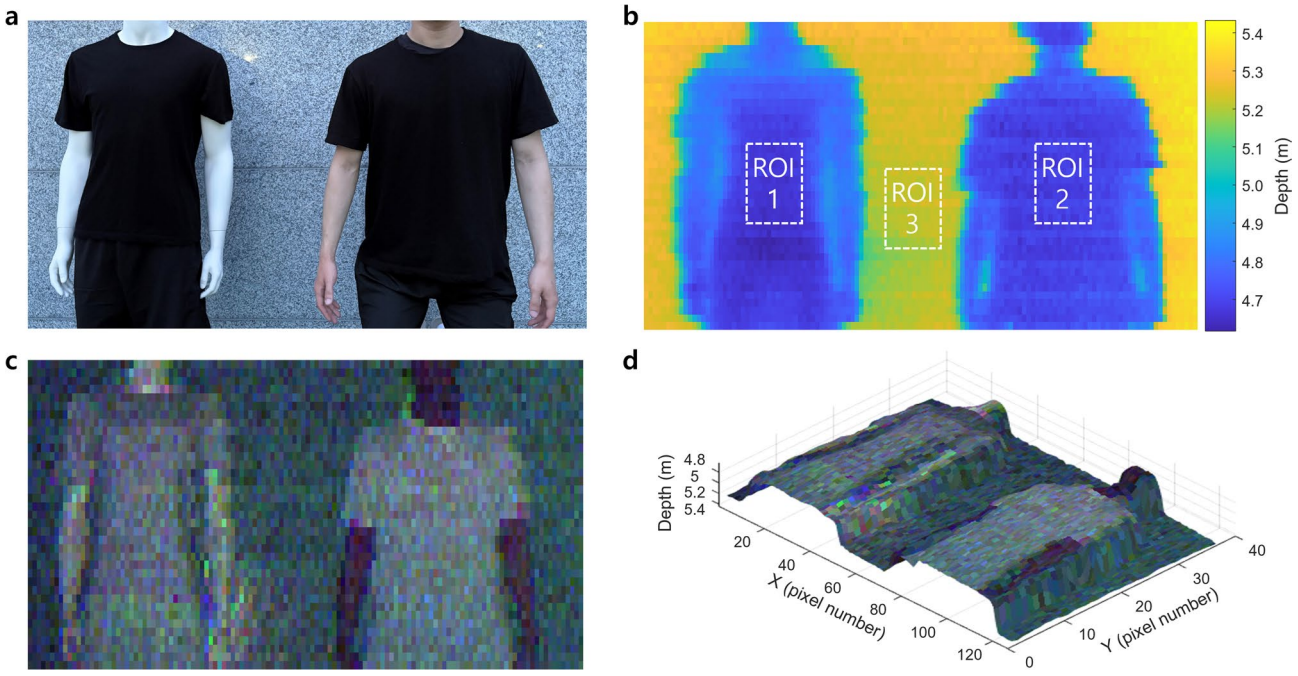

Fig. 6. Dual-domain detection of material characteristics and range information using a multispectral vision system. (**a**) Photograph of the target object measurement scene and comprising a mannequin (left) and a human subject (right). (**b**) Distance map acquired at a 5 m range. (**c**) False-color RGB image generated by combining mapping results from three different wavelengths at a 5 m range. (**d**) Combined dual-domain image integrating both material characteristic mapping and distance information.

representation(Fig. 6d). This fusion of spectral and spatial information provides a useful framework for robotic perception in complex environments. In practical applications, the depth map can be used to determine object shape and position, while the multispectral false-color information can help identify the material type of the target surface, enabling more appropriate grasping and handling decisions.

Conclusions

In summary, this study introduces a spectrometer-free dual-domain machine vision system that employs TDM of nanosecond NIR pulsed lasers to simultaneously acquire spectral and depth information within a compact architecture. By structurally decoupling the ToF ranging and spectroscopic modules, the proposed system achieves high-precision distance measurement and accurate spectral acquisition while minimizing optical loss. The system successfully distinguished 12 visually similar materials, demonstrating that NIR spectral fingerprints encoded as false-color RGB images can be effectively analyzed through a CNN for reliable material recognition. Furthermore, the model exhibited strong generalization capability when applied to unseen geometries and real-world measurements involving human subjects, confirming its robustness and applicability beyond controlled laboratory conditions.

This architecture eliminates the reliance on bulky dispersive optics commonly found in conventional multispectral LiDAR systems, offering a compact, scalable, and efficient alternative for integrated spectral-spatial sensing. Such characteristics make the system particularly attractive for robotic perception, smart manufacturing, and human-robot interaction environments requiring both material awareness and precise geometry reconstruction. Beyond its immediate applications, the demonstrated TDM-based NIR ToF framework establishes a foundation for next-generation high-speed, high-precision machine vision technologies. Moreover, its seamless compatibility with Physical AI paradigms suggests potential use in training autonomous systems within simulated or hybrid environments, ultimately enhancing the intelligence, adaptability, and reliability of future robotic vision platforms.

Data availability

The datasets generated and/or analyzed during the current study are available from the corresponding author on reasonable request.

Received: 14 February 2026; Accepted: 9 April 2026
Published online: 20 April 2026

References

1. Shirmohammadi, S. & Ferrero, A. Camera as the instrument: The rising trend of vision based measurement. *IEEE Instrum. Meas. Mag.* **17**, 41–47 (2014).
2. BinYan, L., YanBo, W., ZhiHong, C., JiaYu, L. & JunQin, L. In *Chin Autom Congr,*. 7277–7281 (IEEE).
3. Manakitsa, N., Maraslidis, G. S., Moysis, L. & Fragulis, G. F. A review of machine learning and deep learning for object detection, semantic segmentation, and human action recognition in machine and robotic vision. *Technologies (Basel)* **12**, 15 (2024).
4. Pérez, L., Rodríguez, Í., Rodríguez, N., Usamentiaga, R. & García, D. F. Robot guidance using machine vision techniques in industrial environments: A comparative review. *Sensors (Basel)* **16**, 335 (2016).
5. Shahria, M. T. et al. A comprehensive review of vision-based robotic applications: Current state, components, approaches, barriers, and potential solutions. *Robotics* **11**, 139 (2022).
6. Xiao, X., Jiang, Y. & Wang, Y. Key technologies for machine vision for picking robots: Review and benchmarking. *Mach. Intell. Res.* **22**, 2–16 (2025).
7. Preethichandra, D., Piyathilaka, L. & Izhar, U. Review on robotic systems for environmental monitoring. *IEEE Open J. Instrum. Meas.* **4**, 1–17 (2024).
8. Nguyen, R. M., Prasad, D. K. & Brown, M. S. In *European Conference on Computer Vision,* 186–201 (Springer).
9. Li, Y., Moreau, J. & Ibanez-Guzman, J. Emergent visual sensors for autonomous vehicles. *IEEE Trans. Intell. Transp. Syst.* **24**, 4716–4737 (2023).
10. Bell, S., Upchurch, P., Snavely, N. & Bala, K. In *Proceedings of the IEEE Conference on Computer Vision and Pattern Recognition,* 3479–3487.
11. Schwartz, G. & Nishino, K. Recognizing material properties from images. *IEEE Trans. Pattern Anal. Mach. Intell.* **42**, 1981–1995 (2019).
12. Wunsch, L., Tenorio, C. G., Anding, K., Golomoz, A. & Notni, G. Data fusion of rgb and depth data with image enhancement. *J. Imaging* **10**, 73 (2024).
13. Zheng, Z. et al. Exploiting scattering-based point spread functions for snapshot 5D and modality-switchable lensless imaging. *Laser Photonics Rev.* **20**, e71005 (2026).
14. Baek, N., Lee, Y., Kim, T., Jung, J. & Lee, S. A. Lensless polarization camera for single-shot full-Stokes imaging. *APL Photonics* https://doi.org/10.1063/5.0120465 (2022).
15. Satav, A. G., Kubade, S., Amrutkar, C., Arya, G. & Pawar, A. A state-of-the-art review on robotics in waste sorting: Scope and challenges. *Int. J. Interact. Design Manuf. (IJIDeM)* **17**, 2789–2806 (2023).
16. Zhang, X., Wang, H. & Dong, H. A survey of deep learning-driven 3D object detection: Sensor modalities, technical architectures, and applications. *Sensors* **25**, 3668 (2025).
17. Ward, I. R., Laga, H. & Bennamoun, M. In *RGB-D Image Analysis and Processing* 169–201 (Springer, 2019).
18. Zhu, B. et al. Surrounding object material detection and identification method for robots based on ultrasonic echo signals. *Appl. Bionics Biomech.* **2023**, 1998218 (2023).
19. Heigl, N. et al. Near infrared spectroscopy for polymer research, quality control and reaction monitoring. *J. Near Infrared Spectrosc.* **15**, 269–282 (2007).
20. Song, H. et al. Short-wave infrared (SWIR) imaging for robust material classification: Overcoming limitations of visible spectrum data. *Appl. Sci. (Basel) (2076-3417)* https://doi.org/10.3390/app142311049 (2024).
21. Manakkakudy, A., De Iacovo, A., Maiorana, E., Mitri, F. & Colace, L. Material classification based on a SWIR discrete spectroscopy approach. *Appl. Opt.* **62**, 9228–9237 (2023).
22. Hansen, M. P. & Malchow, D. S. In *Thermosense Xxx.* 94–104 (SPIE).
23. Hussein, M. E., Spinoulas, L., Xiong, F. & Abd-Almageed, W. In *2018 IEEE International Workshop on Information Forensics and Security (WIFS),* 1–8 (IEEE).
24. Liu, H., Yang, J., Fang, H., Ji, T. & Cai, Z. MSI-RGB dual-source multiscale fusion-based solid waste object detection. *IEEE Trans. Instrum. Meas.* https://doi.org/10.1109/TIM.2024.3480227 (2024).
25. Zheng, Y., Bai, J., Xu, J., Li, X. & Zhang, Y. A discrimination model in waste plastics sorting using NIR hyperspectral imaging system. *Waste Manag.* **72**, 87–98 (2018).
26. Bragato, G., Piccolo, G., Sattier, G. & Sada, C. Identification of spectral responses of different plastic materials by means of multispectral imaging. *Environ. Sci. Process. Impacts* **26**, 802–813 (2024).
27. Singh, M. K., Hait, S. & Thakur, A. Hyperspectral imaging-based classification of post-consumer thermoplastics for plastics recycling using artificial neural network. *Process. Saf. Environ. Prot.* **179**, 593–602 (2023).
28. Song, A. et al. Impact of phase error on coherent Lidar: Analysis and validation. *J. Lightwave Technol.* **43**, 4149–4155 (2024).
29. Li, Y. et al. Hyperspectral imaging through scattering layers with incoherent light. *Appl. Phys. Lett.* **120**, 101101 (2022).
30. Shang, Z. et al. Measurement of gear tooth profiles using incoherent line structured light. *Measurement* **189**, 110450 (2022).
31. Akkoyun, F. Inexpensive multispectral imaging device. *Instrum. Sci. Technol.* **50**, 543–559 (2022).
32. Grönwall, C. et al. In *Electro-Optical Remote Sensing, Photonic Technologies, and Applications VII; and Military Applications in Hyperspectral Imaging and High Spatial Resolution Sensing,* 32–46 (SPIE).
33. Tobin, R., Halimi, A., McCarthy, A., Soan, P. J. & Buller, G. S. Robust real-time 3D imaging of moving scenes through atmospheric obscurant using single-photon LiDAR. *Sci. Rep.* **11**, 11236 (2021).
34. Pan, S. et al. Land-cover classification of multispectral LiDAR data using CNN with optimized hyper-parameters. *ISPRS J. Photogramm. Remote Sens.* **166**, 241–254 (2020).
35. Hopkinson, C., Chasmer, L., Gynan, C., Mahoney, C. & Sitar, M. Multisensor and multispectral LiDAR characterization and classification of a forest environment. *Can. J. Remote Sens.* **42**, 501–520 (2016).
36. Sivaprakasam, V. et al. Multi-spectral SWIR lidar for imaging and spectral discrimination through partial obscurations. *Opt. Express* **31**, 5443–5457 (2023).
37. Chen, Y. et al. Two-channel hyperspectral LiDAR with a supercontinuum laser source. *Sensors-Basel* **10**, 7057–7066 (2010).
38. Song, S. et al. A new waveform decomposition method for multispectral LiDAR. *ISPRS J. Photogramm. Remote Sens.* **149**, 40–49 (2019).
39. Fredell, M., Rahmlow Jr, T., Cote, W., Mann, R. & Johnson Jr, R. In *Free-Space Laser Communications XXXII,* 323–330 (SPIE).
40. Benton, D. M. In *Electro-Optical and Infrared Systems: Technology and Applications XXI,* 58–67 (SPIE).
41. Kim, S. et al. Time division multiplexing based multi-spectral semantic camera for LiDAR applications. *Sci. Rep-Uk* **14**, 11445 (2024).
42. Al Osman, H. & Shirmohammadi, S. Machine learning in measurement Part 2: Uncertainty quantification. *IEEE Instrum. Meas. Mag.* **24**, 23–27 (2021).
43. Tucker, R. S., Eisenstein, G. & Korotky, S. K. Optical time-division multiplexing for very high bit-rate transmission. *J. Lightwave Technol.* **6**, 1737–1749 (2002).
44. Hamilton, S., Robinson, B., Moores, J., Hakimi, F. & Schulz, P. In *Optical Fiber Communication Conference.* WO3 (Optica Publishing Group).
45. Kinsel, T. S. Wide-band optical communication systems: Part I—Time division multiplexing. *Proc. IEEE* **58**, 1666–1683 (2005).
46. Krizhevsky, A., Sutskever, I. & Hinton, G. E. Imagenet classification with deep convolutional neural networks. In *Advances in Neural Information Processing Systems*, Vol. 25 (2012).
47. Long, J., Shelhamer, E. & Darrell, T. In *Proceedings of the IEEE Conference on Computer Vision and Pattern Recognition,* 3431–3440.

Author contributions

T.J., J.K. and S.K. conceived and designed the study. T.J., J.K., A.G. and S.K. designed the optical systems and software. T.J., J.K., E.C., S.K., S.K., M.S. and J.L performed the optical measurements. T.J., J.K., E.C., A.G., R.A.T and S.K. conducted the data analysis. All authors contributed to the preparation of the manuscript.

Funding

This work was supported by Korea Evaluation Institute of Industrial Technology (KEIT) grant funded by the Korea government (MOTIE) (No. 1415181754) and National Research Foundation of Korea (NRF) grant funded by the Korean government (RS-2024-00336583, RS-2023-00236798).

Declarations

Competing interests

The authors declare no competing interests.

Ethics approval

Human involvement in this study was limited to non-medical measurements for system evaluation. No medical or clinical procedures were involved. Formal approval from a named institutional or licensing committee was not required for this work. Informed consent was obtained from the participant prior to the measurements and for publication of the images.

Additional information

Supplementary Information The online version contains supplementary material available at https://doi.org/10.1038/s41598-026-48640-x.

Correspondence and requests for materials should be addressed to S.K.

Reprints and permissions information is available at www.nature.com/reprints.

Publisher's note Springer Nature remains neutral with regard to jurisdictional claims in published maps and institutional affiliations.